

Uncovering Universal Characteristics of Homing Paths using Foraging Robots

Somnath Paramanick ¹, Arup Biswas ², Harsh Soni ^{3,*}, Arnab Pal ^{2,†} and Nitin Kumar ^{1,‡}

¹*Department of Physics, Indian Institute of Technology Bombay, Powai, Mumbai 400076, India*

²*The Institute of Mathematical Sciences, CIT Campus, Taramani, Chennai 600113, India*

and Homi Bhabha National Institute, Training School Complex, Anushakti Nagar, Mumbai 400094, India

³*School of Physical Sciences, Indian Institute of Technology Mandi, Mandi 175001, India*



(Received 26 February 2024; accepted 16 July 2024; published 13 August 2024)

Homing—the incredible ability of animals to navigate back to their homes from unfamiliar places is surprisingly widespread and crucial for their survival. However, the physical understanding of this phenomenon is not yet developed. Here we use a light-controlled robot mimicking foraging and homing behavior to investigate this phenomenon. The robot as a forager is a self-propelled active particle programmed to undergo an in-plane active Brownian (AB) motion whose velocity vector \mathbf{v} undergoes rotational diffusion of magnitude D_r . During the homing phase, the robot undergoes guided motion toward a positive light gradient aided by repeated reorientations, directing it back to its home. Our key finding is an interesting optimal behavior where the mean homing time becomes independent of D_r beyond a critical value posited as a signature of enhanced efficiency. We develop a first-passage-based theoretical model of homing motion, which elucidates this finding as well as accurately captures quantitative features of the homing trajectories in the form of temporal autocorrelation function of the robot's orientation. Inspired by the paradigm of stochastic resetting processes, we also perform an alternative homing motion in a computer, which integrates an AB motion with course correction resets, corroborating our experimental findings. Finally, we test our model on the publicly available data on homing pigeons and capture similar key characteristics of the homing trajectories. Together, these results offer valuable insights into the physics of homing dynamics, providing a statistical basis for its robustness across the animal kingdom.

DOI: [10.1103/PRXLife.2.033007](https://doi.org/10.1103/PRXLife.2.033007)

I. INTRODUCTION

A fundamental aspect crucial for the survival of various animal species is their ability to successfully return home, whether it involves migration, foraging for food, or locating a breeding site. This innate behavior, known as Homing, is surprisingly ubiquitous, allowing animals to navigate back from seemingly unfamiliar locations over considerable distances, and has puzzled scientists over several decades [1,2]. The mechanisms facilitating homing can vary significantly among species which includes path integration (dead reckoning) [3–5], reliance on olfaction [6,7], topographical memory [8–10], and orientation using magnetic or celestial cues [11,12]. Despite this diversity, homing has proven to be an exceptionally successful and efficient process employed by animals. Past research has primarily focused on determining cues that organisms rely on to get the directional information

and how they utilize this information for successful navigation [13–22]. Nonetheless, it remains unclear whether there are universal features in homing dynamics, given its prevalence in nature, and if so, how simple theoretical models can be designed for navigational homing agents to unfold those characteristics. Surprisingly, many of these questions remain unexplored.

Previous studies have shown that organisms' homing times vary widely with factors like age [23,24], climatic conditions [25,26], and even whether the animal is alone or in a group [27–29]. Together, these factors act as sources of stochastic noise in their motion. Moreover, while the physiological mechanisms that underpin homing can vary among organisms, successful homing events require frequent course corrections or directional reorientations during navigation. Thus, the final homing trajectory and time must depend on the interplay between the stochasticity strength and the frequency of reorientations. Elucidating this requires a comprehensive statistical analysis of trajectories traversed by animals undergoing homing with varying strengths of stochasticity in their dynamics. Given the challenges associated with experimenting on living organisms, the use of programmable lifelike robotic particles has emerged as a practical choice for exploring and unraveling the complexities of living organisms [30–34].

In this study, we design programmable robots equipped with the ability to detect physical objects and light gradients. Employing these capabilities, they undergo a search process to locate targets or payloads, followed by homing, where they

*Contact author: harsh@iitmandi.ac.in

†Contact author: arnabpal@imsc.res.in

‡Contact author: nkumar@iitb.ac.in

Published by the American Physical Society under the terms of the Creative Commons Attribution 4.0 International license. Further distribution of this work must maintain attribution to the author(s) and the published article's title, journal citation, and DOI.

return to their home or base. To imitate living dynamics in our robot, we use an active Brownian (AB) model characterized by directed motion of constant speed with superimposed rotational diffusion D_r [35,36]. We use D_r as the parameter that directly measures the stochastic noise in its dynamics along the motion. The robot commences its journey from a designated origin point, which coincides with its home—the region of peak intensity within a radially decreasing light field. During the foraging phase, the robot autonomously searches for a randomly placed object and captures it. The homing phase is where it embarks on the homeward motion. Guided by its light intensity (LI) sensors, the robot performs *tropotaxis*, ensuring it consistently moves towards higher light intensity, aided by repeated stochastic reorientations. This essentially prevents the robot from deviating significantly from the intended direction without making large directional errors.

The central results emanating from our analysis are summarized as follows. We observe the existence of an optimal D_r^* , such that for $D_r < D_r^*$, the homing time monotonically increases with D_r , but for $D_r > D_r^*$, it saturates. The resulting insensitivity to noise beyond D_r^* indicates an enhanced homing efficiency. We also find that D_r^* corresponds to a certain critical reorientation frequency (ν^*), which marks the onset of the observed optimality. Drawing insights from the experiments, we develop a first-passage-based theoretical model that explains the existence of D_r^* and also accurately predicts the nature of the orientation autocorrelation functions of the homing trajectories below and above D_r^* . To explore further, we simulate, in computer, a homing scenario where the orientation of the robot, manifested as an AB particle, is stochastically reset directly pointing towards home. The critical resetting frequency obtained from the simulations matches closely with ν^* , thus providing an alternate scheme for homing dynamics integrated with error corrections. Finally, we analyze the homing trajectories of flocking pigeons from Ref. [28], unveiling striking similarities with our experiments and theory. Together, these experiments reveal new insights into all-prevalent animal homing behavior.

II. ROBOT MODEL

Our robot is a circularly shaped electronic gadget with a diameter of 7.5 cm as described in Ref. [37] [see Fig. 1(a)]. It relies on a differential-drive mechanism where the velocities of two wheels [$v_l(t)$ and $v_r(t)$ in Fig. 1(b)] are controlled independently. It also carries eight infrared (IR) sensors symmetrically placed along the circumference to detect physical objects. It performs tropotaxis using two LI sensors, each placed at the front and back, enabling it to detect intensity gradients along the polarity axis parallel to its wheels.

In this study, we model our robot to perform an AB motion. Here, the magnitude of the robot's in-plane velocity ($|\mathbf{v}|$) remains constant, whereas its orientation $\theta(t)$ undergoes rotational diffusion of magnitude D_r , which can be controlled with great accuracy [37] (see Appendix A). As a result, the robot performs a random motion in the plane with typical trajectories shown in Fig. 1(c) and SM movie S1. Figure S1 in Supplemental Material (SM) [54] explains the procedure of calculating D_r from trajectories. We characterize the motion using spatial velocity autocorrelation function, $C_v(l) =$

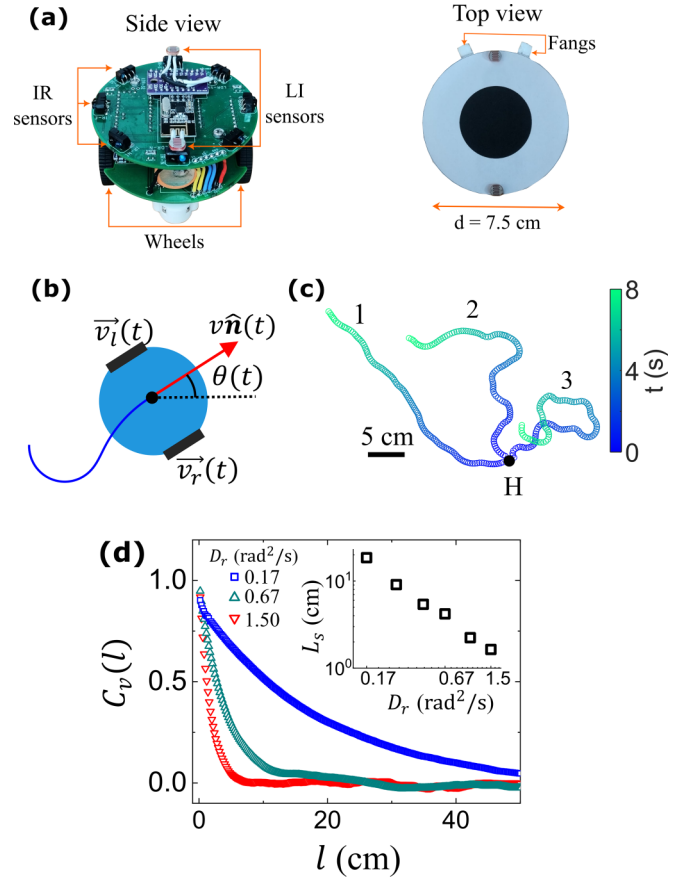


FIG. 1. Robot modeled as an AB particle: (a) Left: Side view of the robot with its important components highlighted. Right: The top view has a paper cover and two fangs that help it grab the payload. We change the printed black pattern on the paper cover depending on the particle tracking requirements. (b) The robot's left and right wheel velocities ($v_l(t)$ and $v_r(t)$, respectively) are modeled such that it moves as an AB particle with constant speed $|\mathbf{v}|$ and rotational diffusion constant D_r . $\hat{\mathbf{n}}(t)$ represents its instantaneous in-plane orientation. (c) Typical trajectories of the robot following in-plane AB dynamics with a constant velocity of 4 cm/s and with D_r of (1) 0.17, (2) 0.67, and (3) 1.50 rad^2/s . (d) Spatial velocity autocorrelation function, $C_v(l)$ shows exponential decay ($\sim e^{-l/L_s}$) for in-plane AB dynamics. Inset: Persistence length, L_s decreases with D_r .

$\langle \mathbf{v}(r) \cdot \mathbf{v}(r+l) \rangle_r / v^2$, where r is the distance traveled, with respect to l for different values of D_r [see Fig. 1(d)]. We find that $C_v(l) \propto e^{-l/L_s}$, where L_s is the persistence length, which is a systematic function of D_r [Fig. 1(d) inset]. In conclusion, by manipulating D_r , we can precisely control the level of randomness in the robot's movements.

III. RESULTS

A. Robot executing active foraging and homing

The experimental scheme is as follows: Our objective is for the robot to independently locate and capture a payload and return it to its initial point or home. Throughout the return (or homing) phase, we seek the robot to make regular course corrections to enhance its navigation towards home.

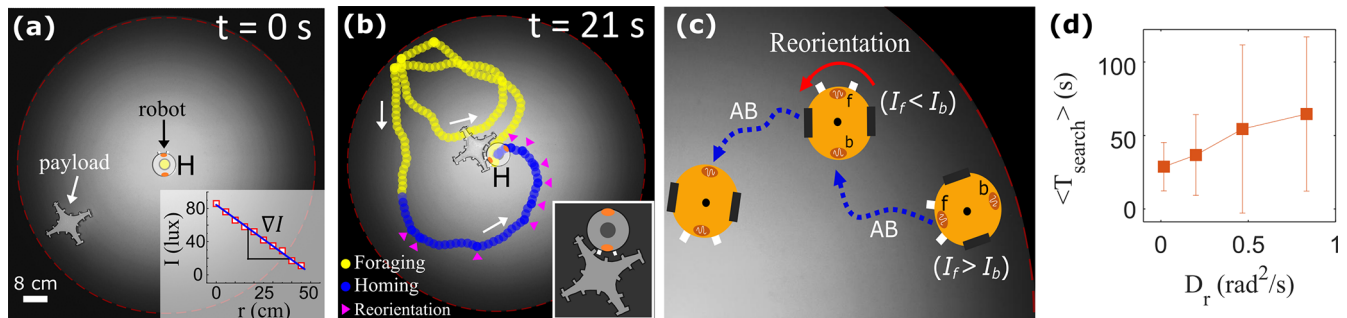


FIG. 2. Robot executing active foraging and homing: (a) At $t = 0$ s, The robot is placed at the center region H , which is the brightest region of the radially symmetric light-intensity gradient field of magnitude ∇I (inset). The red dashed line at the circumference defines the boundary, characterized by a sudden fall in intensity. (b) The robot performs an AB motion (yellow trajectory, $v = 10$ cm/s and $D_r = 0.15$ rad²/s) and searches for the payload randomly. Kinks in the trajectory indicate reflections from the boundary. The return trajectory (blue line) is the same as the search AB motion, except that every time the robot points in the direction of decreasing intensity, it undergoes reorientation until it again points toward increasing intensity. Magenta arrowheads represent such events. Inset: Fangs stay latched to cogs during the robot's return. (c) A schematic of a typical reorientation event. f and b indicate the front and the back LI sensors with intensity readings of I_f and I_b , respectively. If during the journey $I_f < I_b$, the robot undergoes a reorientation represented with a red arrow until $I_f > I_b$ again. Its dynamics between the two such events remain AB. (d) The mean search time of the foraging AB robot calculated over 100 trajectories increases with D_r . Error bars represent standard deviation.

We will examine whether the number of course corrections made during homing impacts the total homing time.

We begin by confining the robot inside a region illuminated by an overhead projector, which is a circle of diameter 1 m [Fig. 2(a), SM movie S2 [54]]. The intensity of light, I , measured in *lux*, decreases radially at a rate ∇I [inset of Fig. 2(a)]. The region H , which we call home, lies at the center of the circle, which also corresponds to the brightest region in the plane. During the foraging phase, the robot starts from H and performs an AB motion with $v = 10$ cm/s and $D_r = 0.02$ – 1.24 rad²/s. To avoid its escape, we program it to reflect from the boundary wall, indicated with a red dashed line in Fig. 2(a), beyond which there is a sharp fall in the light intensity. Such reflection events can be seen in the yellow trajectory in Fig. 2(b). During the search phase, the robot's IR sensors continuously emit IR radiation. The payload (cut out from a piece of styrofoam) is deemed searched when the robot is close enough to detect the reflected IR signal from the payload, with the robot now pushing onto the payload due to its persistent AB motion. Additionally, the concavity of the payload's surface makes sure that the robot remains locked to it, a phenomenon equivalent to the funnel trapping of active particles reported in the past [38–40]. Simultaneously, the robot activates its front and back LI sensors, indicated by orange dots [see Fig. 2(b) inset]. The average search time $\langle T_{\text{search}} \rangle$, defined as the time taken by the robot to detect the payload using its IR sensors during the foraging phase [yellow trajectory in Fig. 2(b)] increases with D_r along expected lines [Fig. 2(d)].

The robot is now set to perform the homing motion. During homing, it uses LI sensors to detect the local light intensity at its front and back, I_f and I_b , respectively [Fig. 2(c)], to undergo tropotaxis motion. While $I_f > I_b$, the robot continues to perform the AB motion. However, when $I_f < I_b$, it reorients itself [red arrow in Fig. 2(c)] until $I_f > I_b$ again and resumes its AB motion (see SM movies S2 and S3 [54]). This is reminiscent of the wide range of taxis mechanisms employed by organisms for directed movement [1,2]. We perform all

experiments at $|\nabla I| = 1.54$ lux/cm where the sensors are most accurate such that they never make errors in I_f and I_b measurement. Note that the exact functional form of the gradient is unimportant for experiments as long as it exhibits a monotonic dependence on the radial distance. Also, the nudge provided by the reorientation is incremental, offering a slight tweak in the robot's direction rather than a sharp turn, as one would expect in real organisms. Each reorientation event takes a finite time of t_r in experiments, a variable in the robot's program. When reorienting, the two fangs attached to the robot get interlocked to the cogs on the payload surface and ensure that they never detach [inset of Fig. 2(b)]. The process continues until the robot reaches H , with a blue curve indicating the complete homing trajectory [Fig. 2(b)]. The magenta arrowheads indicate reorientation events.

Quite remarkably, with an initial condition of the payload always kept at the boundary and the robot pointing directly toward H , we find that mean homing time $\langle T \rangle$, averaged over 100 experiments, increases linearly with D_r initially but saturates to a fixed value of ≈ 8.2 s for $t_r = 0.3$ s and ≈ 15 s for $t_r = 1$ s, respectively, beyond critical $D_r^* \approx 0.46$ rad²/s [see Fig. 3(a)]. The error bars measure the standard deviation of the T distribution (see SM Fig. S2 [54] for the detailed data). In other words, the homing time remains optimal irrespective of the value of stochastic noise, underscoring the efficiency of the process. We can further define $\langle T_0 \rangle \equiv \langle T - nt_r \rangle$, where n represents the number of reorientation events in a single trajectory. Thus, $\langle T_0 \rangle$ can be regarded as the mean homing time with instantaneous reorientations, which shows similar optimality as the finite t_r case [see Fig. 3(b)].

To understand the role played by reorientations, we plot their average number, $\langle n \rangle$, during the homing phase for various D_r values in Fig. 3(c). We find that $\langle n \rangle$ monotonically increases with D_r , well beyond D_r^* . Using this, we define an average reorientation rate $\nu \equiv \langle n \rangle / \langle T_0 \rangle$. Note that there is a ν corresponding to every D_r as shown in Fig. 3(d). Also, the time interval between consecutive reorientations is shown to follow an exponential distribution [Fig. 3(e)], and the

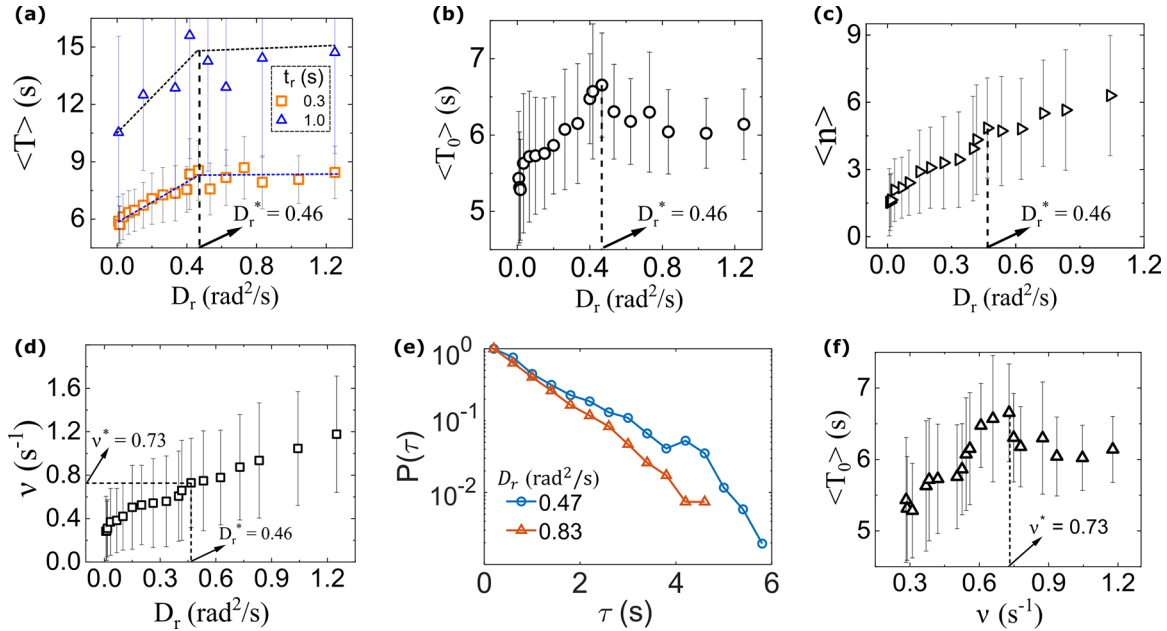


FIG. 3. Experimental observation of optimal homing time: (a) The mean homing time, $\langle T \rangle$, for two values of reorientation times, t_r , increases linearly with D_r up to $D_r^* = 0.46 \text{ rad}^2/\text{s}$, beyond which it becomes almost constant. The averaging is performed over 100 experiments with dashed lines representing a guide to the eye. (b) Average homing time $\langle T_0 \rangle$ with instantaneous reorientations ($t_r = 0$) shows a linear increase for low D_r and becomes constant at higher D_r as predicted by the theoretical model [Eqs. (3) and (4)]. (c) and (d) The average number of reorientation events, $\langle n \rangle$, and the corresponding reorientation rate $\nu \equiv \langle n \rangle / \langle T_0 \rangle$ increasing linearly with D_r , respectively. (e) The distribution of time between two consecutive reorientations (τ) shows an exponential decay. (f) $\langle T_0 \rangle$ shows a maximum at $\nu^* = 0.73 \text{ s}^{-1}$, which corresponding to $D_r^* = 0.46 \text{ rad}^2/\text{s}$ mentioned in (a) and (b). Error bars equal the standard deviation (SD) in all plots.

empirical rate has an inherent distance dependence albeit weak (see SM Fig. S3 [54]). Using this information, we plot $\langle T_0 \rangle$ as a function of ν [Fig. 3(f)]. Interestingly, its maximum lies at $\nu^* = 0.73 \text{ s}^{-1}$, which corresponds to the D_r^* beyond which the homing time showed saturation in Figs. 3(a) and 3(b). Therefore, D_r^* corresponds to the effective reorientation frequency beyond which the homing time becomes optimum.

To gain further insights, we compare typical homing trajectories for D_r below and above D_r^* , as shown in Figs. 4(a) and 4(b), respectively (also SM movie S4 [54]). For convenience, we conduct these experiments without having the robot carry the payload. For $D_r < D_r^*$ ($D_r = 0.02 \text{ rad}^2/\text{s}$), the trajectories exhibit strong persistence with few reorientations represented by magenta arrowheads for one typical trajectory, gradually spiraling towards H [Fig. 4(a)]. In contrast, for $D_r > D_r^*$ ($D_r = 0.83 \text{ rad}^2/\text{s}$), the trajectories maintain overall persistence towards H due to frequent reorientation events with stochastic noise limited to short timescales [Fig. 4(b)]. We quantify the tortuosity of trajectories by calculating the temporal autocorrelation function of the robot's orientation, $C_\theta(t) = \langle \hat{\mathbf{n}}(0) \cdot \hat{\mathbf{n}}(t) \rangle$. Here, $\hat{\mathbf{n}}(t)$ represents the unit vector along the robot's orientation at time t and angular brackets denote averaging over 350 trajectories. For $D_r = 0.02 \text{ rad}^2/\text{s}$, $C_\theta(t)$ shows a linear decay as a function of time [Fig. 4(c), solid line]. On the contrary, for $D_r = 0.83 \text{ rad}^2/\text{s}$, it decays initially before saturating to a significant nonzero value. Thus, the characteristics of homing trajectories can be quantified using the functional form of $C_\theta(t)$, which exhibits distinct behavior below and above the critical diffusivity D_r^* .

B. Theoretical analysis

We now present a simple theoretical model to explain certain key features emerging from our experiments. For the sake of continuity, we only present the most relevant results here, skipping the details to Appendix D. Since we are interested in the homing phase, let us denote the fluctuating homing time as T_0 (ignoring the time taken by the reorientation events, i.e., $t_r = 0$) for a single trajectory. For each homing event, the distance R covered by the robot from the starting point to the home can be written as

$$R = \int_0^{T_0} v \cos \phi(t) dt, \quad (1)$$

where $\phi(t)$ is the angle between the particle's orientation vector $\hat{\mathbf{n}}(t)$ and its instantaneous radial distance $r(t)$ from the home at a time t (see Fig. 5 inset). Averaging the above equation over the stochastic dynamics for a fixed R , we can approximately write the following equation

$$R \simeq \int_0^{\langle T_0 \rangle} v \langle \cos \phi(t) \rangle dt. \quad (2)$$

In our experiments, the choice of the initial condition for the robot's orientation implies $\phi = 0$ at $t = 0$. In the small D_r limit, i.e. when the persistence time is much larger than the homing time $D_r^{-1} \gg \langle T_0 \rangle$, the mean-square deviation of $\phi(t)$ is approximately $2D_r t$, so $\phi(t)$ typically remains within a narrow range of size $\Delta\phi \simeq 2\sqrt{2D_r t}$ around $\phi = 0$, leading to $\langle \cos \phi(t) \rangle \simeq 1 - D_r t$ (see Appendix D). In this case, the

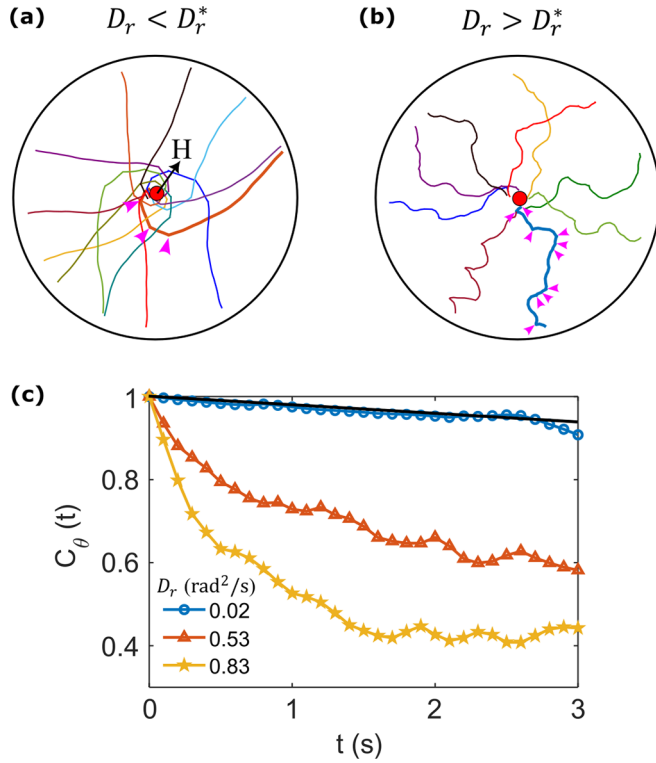


FIG. 4. Insights into the homing trajectories using temporal orientation autocorrelation function: (a) Typical homing trajectories of the robot with $D_r = 0.02 \text{ rad}^2/\text{s}$ starting from the boundary with an initial orientation toward home (H) showing more persistence over short timescales and spiraling toward home. (b) Conversely, trajectories with $D_r = 0.83 \text{ rad}^2/\text{s}$ are noisier at short timescales yet maintain an overall propensity to move towards H . Magenta arrowheads on the bolder trajectories denote the locations of reorientation events. (c) Temporal orientation autocorrelation function, $C_\theta(t)$ averaged over 350 homing trajectories for different D_r values plotted as a function of time. For trajectories shown in (a), it decays linearly with a slope of $-D_r$ (solid line). For trajectories shown in (b), $C_\theta(t)$ decays rapidly initially but saturates to a smaller yet finite value.

average number of reorientation events is small for small D_r [see Fig. 3(c)] and mostly occurs towards the end of the homing phase [Fig. 4(a)]. Substituting the expectation in Eq. (2) and by readjusting, we obtain the following expression for the mean homing time

$$\langle T_0 \rangle \simeq \frac{R}{v} \left(1 + \frac{R}{2v} D_r \right), \quad (3)$$

which exhibits a linear relation with D_r , as observed in our experiments [see Fig. 3(b) for $D_r < D_r^*$].

For large values of D_r , one should have $D_r^{-1} \ll \langle T_0 \rangle$ such that ϕ often reaches the maximum allowed range between $[-\pi/2, \pi/2]$. This is easy to see as in experiments $I_f = I_b$ corresponds to the scenario $\phi = \pm\pi/2$. Note, however, that $I_f < I_b$ is forbidden in experiments, thus restricting $|\phi(t)| \leq \pi/2$. It is thus reasonable to consider that ϕ always remains confined to the range $[-\pi/2, \pi/2]$. Starting from an initial condition at $t = 0$, the angle ϕ diffuses and spreads out rapidly within the range $[-\pi/2, \pi/2]$. Assuming ϕ to remain approximately uniform across this range, we get $\langle \cos \phi(t) \rangle \simeq 2/\pi$.

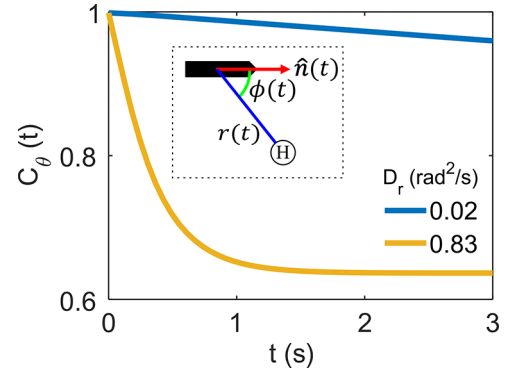


FIG. 5. Theoretical model: $C_\theta(t)$ vs t , obtained from the first-passage theory for $D_r = 0.02$ and $0.83 \text{ rad}^2/\text{s}$ [Eqs. (8) and (7), respectively] indicated with blue and yellow lines, respectively. The curves show a qualitative match with experimental results [Fig. 4(c)]. The inset shows a schematic representation of variables and parameters used in theory.

Substituting this into Eq. (2) yields a D_r -independent average homing time given by

$$\langle T_0 \rangle \simeq \frac{\pi R}{2v}, \quad (4)$$

explaining the saturation of $\langle T_0 \rangle$ for $D_r > D_r^*$ observed in experiments [see Fig. 3(b)].

We now investigate the impact of reorientation events on the temporal orientation autocorrelation function $C_\theta(t) = \langle \cos[\theta(t) - \theta(0)] \rangle$. Skipping details from Appendix D, it is possible to show that $\phi(t)$ follows the stochastic dynamical equation

$$\frac{d\phi}{dt} = \frac{v}{r} \sin \phi + \zeta(t), \quad (5)$$

where $\zeta(t)$ is the rotational noise with the following statistical properties:

$$\begin{aligned} \langle \zeta(t) \rangle &= 0, \\ \langle \zeta(t)\zeta(t') \rangle &= 2D_r \delta(t - t'). \end{aligned} \quad (6)$$

In the large D_r limit, the noise (second) term dominates over the first term and we simply have $d\phi/dt \simeq \zeta(t)$. Thus, ϕ and θ follow the same equation (A1c) and therefore, $\cos[\theta(t) - \theta(0)] \simeq \cos \phi(t)$. Again, using the fact that ϕ remains uniformly distributed in the range $[-\pi/2, \pi/2]$, we find (Appendix D)

$$\begin{aligned} C_\theta(t) &\simeq \langle \cos \phi(t) \rangle \\ &\simeq \frac{2}{\pi} \left[1 + 2 \sum_{n=1}^{\infty} \frac{(-1)^{n-1}}{4n^2 - 1} \exp(-4n^2 D_r t) \right], \end{aligned} \quad (7)$$

which saturates to $2/\pi$ as t increases.

This explains the saturation of $C_\theta(t)$ observed in our experiments for large D_r [see Figs. 4(c) and 5]. On the other hand, in the small D_r limit, $\phi(t)$ remains in the narrow range around $\phi = 0$ as mentioned before, resulting in $\langle \cos \phi(t) \rangle = 1 - D_r t$. As a result, we find

$$C_\theta(t) \simeq 1 - D_r t, \quad (8)$$

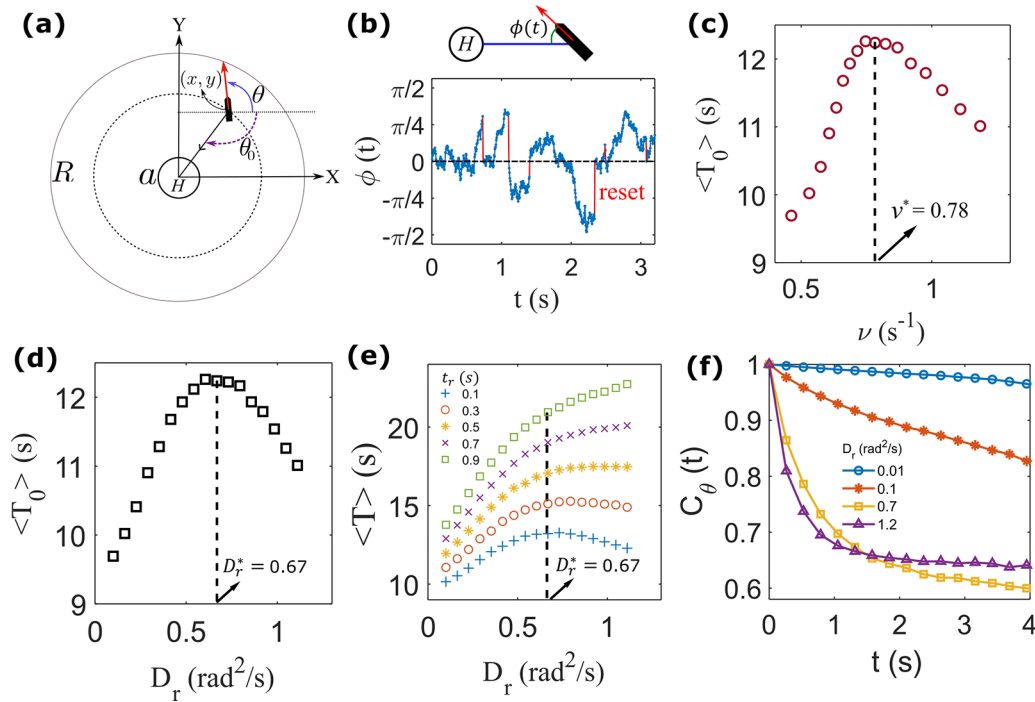


FIG. 6. Stochastic resetting simulation: (a) The position and the orientation of the AB particle with certain D_r at time t is denoted by (x, y) and θ , respectively. Its orientation is stochastically reset to θ_0 with a reset rate of ν . Both D_r and ν are taken from the experimental data presented in Fig. 3(d). The reset continues until the particle reaches home (circle of radius a centered at H). (b) A typical fluctuating trajectory of the particle's instantaneous orientation $\phi(t)$, measured with respect to the radial axis connected H , with intermittent resets to zero. [(c) and (d)] The mean homing time $\langle T_0 \rangle$ as a function of ν and D_r , respectively. The behavior of the homing time and the optimal rate are commensurate with the experimental result in Fig. 3(f) and 3(b), respectively. (e) On addition of time t_r per reset, the homing time shows qualitatively similar behavior as observed in experiments in Fig. 3(a) with the transition $D_r^* = 0.67 \text{ rad}^2/\text{s}$ remaining independent of t_r . (f) Temporal orientation autocorrelation function $C_\theta(t)$ matches well with our theoretical model for low and high D_r values [Eqs. (8) and (7), respectively].

which implies it decays linearly in time with slope $-D_r$ concurring with our experimental observations [see Fig. 4(c) and Fig. 5].

Concluding this part, our theoretical analysis accurately reproduces the observed homing time optimality as well as captures the key features of $C_\theta(t)$ of the homing trajectories. Note that for large D_r , the exact saturation values of both $\langle T_0 \rangle$ and $C_\theta(t)$ observed in experiments will depend on the details of the ϕ distribution [see Appendix E, Eqs. (E1) and (E2)].

C. Homing through stochastic resetting

Notably, the homing process bears a close resemblance to the stochastic resetting-induced first passage time optimization problems [41–47]. As such, by repeatedly resetting a state (could be a spatial coordinate, momentum, external perturbation or phase) to a known or random configuration, one can unveil new pathways, avoid potential obstacles. This has been shown to be a very effective mechanism for maximizing search efficiency in various physical, chemical, and biological systems (see Refs. [44,45] for a review on the topic). In our experiments, resetting originates from the self-reorientation events in the robot's trajectory through the intensity difference and not through an external clock, as traditionally done in these existing studies. To understand this better, we propose a theoretical toy model consisting of an AB

particle (with rotational diffusion constant D_r) that mimics the robot under resetting dynamics. The particle starts its motion from the boundary of a circle of radius R and points towards the target which is a circular region of radius a as shown in Fig. 6(a). The parameter a is inspired by the fact that point H , referred to as the home in experiments, has a finite width (see Appendix C). Here we use $R = 46.25 \text{ cm}$ and $a = 2.5 \text{ cm}$. Integrated into the AB motion, the particle undergoes orientational resetting with a reset rate ν , i.e., the instantaneous orientation $\theta(t)$ is reset to a certain direction θ_0 , which orients the angle of movement radially inward, pointing towards the center [see Fig. 6(a) and Appendix F for details] [48,49]. Depending on the particle's exact location in phase space, the resetting angle θ_0 is computed, and the particle is reoriented, following which the underlying active dynamics continues. Consequently, the instantaneous angle $\phi(t)$ of the particle, measured with respect to the radial axis connected to home H , fluctuates and resets to zero [see Fig. 6(b)]. Thus, the phase space coordinates (x, y) do not reset directly in time; rather they are only implicitly affected through the orientation.

The rotational diffusion constant D_r of the simulation particle and the corresponding orientational resetting rate ν are taken from the parameter set presented in Fig. 3(d), which are extracted from the experiments. Thus, the intensity-driven reorientation events in the experiments are interpreted as externally modulated resetting events in simulations, where the

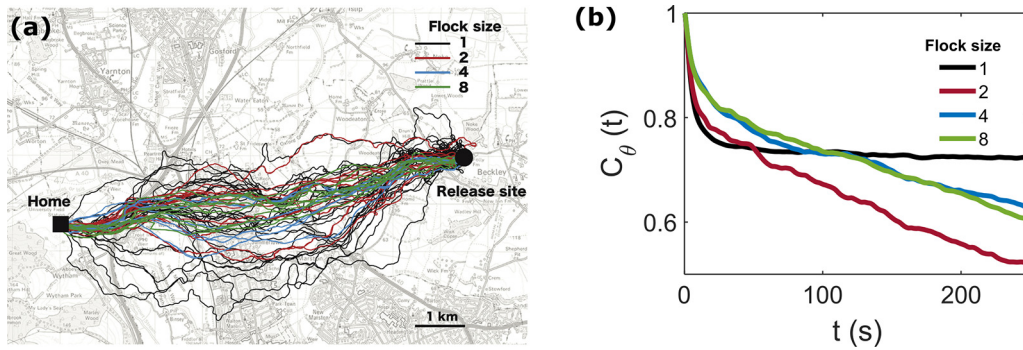


FIG. 7. Applying the homing model on flight trajectories of flocking pigeons: (a) Homing trajectories of solo and flocking pigeons of different sizes between the home and release site; figure adapted from Ref. [28]. (b) $C_\theta(t)$, averaged over multiple trajectories, showing linear decay for flocking birds' trajectories and saturation for solo trajectories at large times, which is in qualitative agreement with experimental and theoretical results obtained for low and high D_r values, respectively. See Fig. 4(c) and Fig. 5 for comparison.

resetting rates are taken empirically from the experiments. Note that in experiments, light-gradient-driven reorientations guarantee that the robot never points away from home. However, in simulations, the particle is free to orient and move in any direction due to its AB motion in the plane. Thus, it is only natural to reset the particle pointing directly towards home. For the same reason, we also ignore the fact that in experiments, v depends on the distance from home (SM Fig. S3 [54]) as discussed before. The homing process continues until the particle reaches within a radius a around the origin. The mean return time to home, $\langle T_0 \rangle$, from this modeling is shown in Fig. 6(c), clearly reproducing the existence of critical reset rate $\nu^* = 0.78 \text{ s}^{-1}$. This also implies the existence of a unique $D_r^* = 0.67 \text{ rad}^2/\text{s}$ [Fig. 6(d)], as also seen in our experiments and predicted from the theoretical analysis. Note that the decreasing trend in $\langle T_0 \rangle$ beyond ν^* and D_r^* is not in contradiction of experiments [Fig. 3(b)] and theory [Eq. (4)] but a direct consequence of the width of the ϕ distribution in simulation, which becomes progressively narrow as D_r increases beyond D_r^* (see SM Fig. S4 [54] and Appendix E).

To incorporate the finite reorientation time which is intrinsic to the robots in simulations, we introduce an overhead time t_r per reset. We vary t_r between 0.1 and 0.9 s and plot the mean homing time $\langle T \rangle$ as a function of D_r in Fig. 6(e). Interestingly, we find $D_r^* = 0.67 \text{ rad}^2/\text{s}$ remains independent of t_r , similar to experimental observation [Fig. 3(a)]. Also, $C_\theta(t)$ in Fig. 6(f) also shows qualitatively similar dependence on D_r , linear decay for $D_r \ll D_r^*$ and saturation at $D_r \gg D_r^*$, as observed in experiments and predicted by our theoretical model [Eqs. (7) and (8), Fig. 4(c), and Fig. 5]. Moreover, the saturation value of $C_\theta(t)$ for high D_r increases with increasing D_r which is consistent with theoretical prediction (see Appendix E). Thus, inspired by the active dynamics models under resetting, we can capture a similar first passage time optimization phenomenon as demonstrated by the foraging and homing active robots.

D. Application of the robot-homing model on a real living system

Finally, we test our predictions on a living system. Our findings indicate that beyond a certain critical value of D_r , the homing time becomes constant and the process remains

equally efficient, irrespective of the increasing strength of the noise. Clearly, measuring D_r directly in a natural living system is difficult, making direct verification of this result unrealistic. However, our model provides an important prediction regarding the functional form of $C_\theta(t)$ for different D_r values. Therefore, analyzing real trajectories of homing organisms offers a practical method to test our model.

To this end, we use a controlled experiment performed by Takao Sasaki *et al.* [28] on homing pigeons *Columba livia* flying in flock sizes of variable numbers as a model system. Their results, using global positioning system (GPS) tracking of the flight tracks, demonstrated that the pigeons flying in larger flocks follow much straighter and more direct flight paths toward home as compared to the birds flying solo (see Fig. 7(a), adapted from the original paper [28]). Since pigeons fly over distances of close to 8 km, they can be assumed to execute AB motion in two dimensions with constant speed [28]. Moreover, it is reasonable to assume that pigeons adjust their rotational diffusion coefficient (D_r) based on flock size, with the highest D_r when flying solo and the lowest D_r in larger flocks. Using trajectory data obtained from the original paper, we compute $C_\theta(t)$ (see Appendix G for details), and find that the behavior closely matches our theoretical predictions [see Fig. 7(b)]. Specifically, pigeons flying in flocks exhibit a linear decay in $C_\theta(t)$, while for solo pigeons, it saturates to a finite value. This provides strong pragmatic evidence that our system of foraging & homing robots can well explain key homing features observed in real-world living systems.

IV. CONCLUSION AND PROSPECT

Drawing inspiration from the homing observed in animals, we employed a programmable self-propelled robot to execute the task resembling foraging and homing. Our objective was to explore the interplay between the inherent randomness in their dynamics and the frequent course corrections observed in homing trajectories. We modeled the homing robot as an active Brownian particle with a rotational diffusion constant (D_r), programed to navigate towards a predefined location guided by light-gradient-driven reorientations. Our observations revealed the presence of an optimal reorientation rate ν^* determined by the inherent noise, D_r^* . Beyond this threshold, the average homing time became largely independent of D_r ,

indicating that animals may have a finite upper limit on return times. Motivated by experimental findings, we developed a theoretical model describing the stochastic evolution of the robot's orientation vector with respect to its radial direction with the home as the center. Our calculations provide an explanation of the presence of D_r^* , and also uncover key differences in the shape of homing trajectories quantified through temporal orientation autocorrelation functions. We further present our results through the lens of the theoretical framework based on the optimization of the first-passage time under stochastic resetting. Specifically, we used the experimentally determined reorientation rate for each D_r as the input reset rate of particle orientation toward the home. Interestingly, our simulations reproduced the experimental findings, indicating that the observed optimality originated due to the stochastic reorientation of the robot as a mode of course correction. Finally, we successfully validate our findings in a system of a homing flock of pigeons with temporal orientation autocorrelation functions extracted from trajectories, showing an excellent qualitative match with our theoretical predictions.

Overall, the results obtained here provide a statistical basis for the remarkable success of homing as a ubiquitous navigational technique adopted by living organisms. Future research will determine how these proposed locomotive homing dynamics can be generalized as a tool to further elucidate the fascinating phenomenon of homing in the fields of biology and ecology [50]. Another important direction for the future is altering our experimental setup to investigate generic homing behaviours where the homing cue is not as simple as a gradient pointing toward home. Our robots have the ability to perform various stochastic dynamical paths featuring correlated diffusion processes on short timescales and diffusion on large timescales [37]. Also, while homing, using their on-board sensors, the robots can adapt different navigational strategies based on environmental cues or other social agent-agent interactions. Given such versatility in the navigational dynamics, we can address several homing time optimization problems with regard to designing an efficient switching strategy and characterizing the robustness in noisy optimal homing paths.

ACKNOWLEDGMENTS

N.K. acknowledges financial support from Department of Science and Technology, India, SERB for Core Research Grant No. CRG/2020/002925 and IITB for the seed grant. A.P. acknowledges research support from the Department of Science and Technology, India, SERB Start-up Research Grant No. SRG/2022/000080 and the Department of Atomic Energy, India. H.S. acknowledges Department of Science and Technology, India, SERB for the Start-up Research Grant (Grant No. SRG/2022/000061-G). S.P. thanks CSIR India for research fellowship [File no: 09/087(1040)/2020-EMR-I]. The numerical calculations reported in this work were carried out on the Nandadevi and Kamet clusters, which are maintained and supported by the Institute of Mathematical Science's High-Performance Computing Center. S.P. and N.K. thank Takao Sasaki for providing valuable details on the bird trajectory data.

S.P. and N.K. designed the research, S.P. performed experiments and analyzed data. H.S. and A.P. developed the

ABP based analytical model. A.B., H.S., and A.P. designed resetting based theoretical modeling and simulations, A.B. performed the latter. All the authors contributed in writing the paper.

APPENDIX A: MODELING THE ROBOT TO FOLLOW AB MOTION

In general, the equations of motion for the robot are given by

$$\dot{x}(t) = v(t) \cos \theta(t), \quad (\text{A1a})$$

$$\dot{y}(t) = v(t) \sin \theta(t), \quad (\text{A1b})$$

$$\dot{\theta}(t) = \zeta(t), \quad (\text{A1c})$$

where $v(t)$ is the robot's speed along its instantaneous orientation $\hat{\mathbf{n}}(\mathbf{t}) = (\cos \theta(t), \sin \theta(t))$. Here $v(t) = (v_l(t) + v_r(t))/2$ and $\zeta(t) = (v_r(t) - v_l(t))/d$ in terms of the robot's instantaneous left and right wheels' velocities v_l and v_r , respectively, with d the diameter of the robot. For mimicking the AB motion, $v_l(t)$ and $v_r(t)$ are varied such that $v(t)$ remains constant and the value of ζ is updated discretely from a uniform distribution between $[-\eta, \eta]$ after every ϵ seconds. For the timescales much larger than ϵ ,

$$\langle \zeta(t)\zeta(t') \rangle = 2D_r \delta(t - t'), \quad (\text{A2})$$

where D_r is the rotational diffusion constant. It is straightforward to show that [51]

$$\langle [\theta(\tau) - \theta(0)]^2 \rangle = 2D_r \tau. \quad (\text{A3})$$

Here the angular bracket represents the ensemble average. Whereas, from the discrete form of (A1c),

$$\theta(\tau) = \theta(0) + \epsilon \sum_{i=1}^{N_\tau} \zeta_i, \quad (\text{A4})$$

where $\zeta_i \equiv \zeta(i\epsilon)$ and $N_\tau = \tau/\epsilon$. As the random number ζ_i has the uniform probability distribution between $[-\eta, \eta]$,

$$\langle \zeta_i \zeta_j \rangle = \delta_{ij} \frac{\eta^2}{3}. \quad (\text{A5})$$

Then, from (A4),

$$\begin{aligned} \langle [\theta(\tau) - \theta(0)]^2 \rangle &= \epsilon^2 \sum_{i=1}^{N_\tau} \sum_{j=1}^{N_\tau} \langle \zeta_i \zeta_j \rangle \\ &= \epsilon \tau \frac{\eta^2}{3}. \end{aligned} \quad (\text{A6})$$

Comparing the above equation with (A3), we obtain

$$D_r = \epsilon \frac{\eta^2}{6}. \quad (\text{A7})$$

Using the above relation, we can control the value of D_r by varying ϵ or η .

APPENDIX B: IMAGE ACQUISITION AND ANALYSIS TECHNIQUE

While capturing video of the robot's movement, we cover its components (except the light intensity sensors) with a

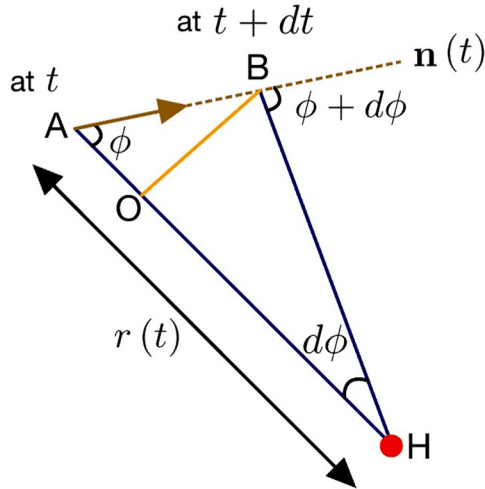


FIG. 8. A schematic that demonstrates the relation between θ and ϕ pertaining to the origin of Eq. (D1b).

white paper cap with a black circle drawn on top of it at the center. We then use the in-house MATLAB code to extract the in-plane instantaneous position coordinates of the robot. The experimental movies were captured at a rate of 10 frames per second.

APPENDIX C: EXPERIMENTAL VALUES OF R AND a

In this study, the robot operates within a circular arena with a diameter of 1 m, with the home position, H , located at the center. The robot begins its homing motion from the circumference. However, to ensure that both its front and back LI sensors remain inside the circle, the effective homing distance, R , is reduced by the robot's radius ($= 3.75$ cm). Thus, $R = 46.25$ cm instead of 50 cm in the experiments. Additionally, since the robot detects the home position as the area of highest intensity through its LI sensors, it is not a single point but a region with a finite width, a . Experimental findings indicate that $a \approx 2.5$ cm.

APPENDIX D: DETAILED ANALYSIS OF THE THEORETICAL MODEL: MEAN HOMING TIME AND TEMPORAL ORIENTATION AUTOCORRELATION FUNCTION

The equations of motion of the robot during the homing phase in terms of its distance $r(t)$ from home and the angle $\phi(t)$ with respect to the axis joining its instantaneous location to its home read

$$\frac{dr}{dt} = -v \cos \phi(t), \quad (\text{D1a})$$

$$\frac{d\phi}{dt} = \frac{v}{r} \sin \phi + \frac{d\theta}{dt}, \quad (\text{D1b})$$

where v denotes the speed of the robot, and θ represents the orientation angle of the robot relative to the x axis of the laboratory frame. As shown in Fig. 8, the change in angle ϕ due to the translational motion of the robot in time dt , in the

$dt \rightarrow 0$ limit, is given by

$$\frac{OB}{OH} = \frac{AB \sin \phi}{AH - AB \cos \phi} = \frac{v \sin \phi dt}{r - v \cos \phi dt} \simeq \frac{v \sin \phi dt}{r}.$$

This leads to the first term in the ϕ equation. The dynamics of θ is governed by the Eq. (A1c) in a standard way.

In our experiments, the robot reorients itself whenever it interacts with the light, and it does not move during reorientation. In the theoretical analysis, we ignore the overhead time taken for these reorientation events. Let T_0 be the random homing time for a single trajectory. Integrating Eq. (D1a) over the homing trajectory, we obtain

$$R = \int_0^{T_0} v \cos \phi(t) dt, \quad (\text{D2})$$

where R is the initial distance of the robot from home which is kept fixed. Taking the ensemble average of the above equation

$$R = \left\langle \int_0^{T_0} v \cos \phi(t) dt \right\rangle, \quad (\text{D3})$$

and further making a mean-level approximation that $T_0 \simeq \langle T_0 \rangle$, we can write

$$R \simeq \int_0^{\langle T_0 \rangle} v \langle \cos \phi(t) \rangle dt. \quad (\text{D4})$$

For $D_r \ll 1/\langle T_0 \rangle$, it is safe to assume that the values of $\phi(t)$ do not deviate much from its initial value $\phi(0) = 0$. Thus, at time t , the mean-square deviation of ϕ would be roughly $2D_r t$. Then, the ensemble average $\langle \cos \phi(t) \rangle$ can be calculated as follows:

$$\begin{aligned} \langle \cos \phi(t) \rangle &\simeq \left\langle \left[1 - \frac{\phi(t)^2}{2} \right] \right\rangle \\ &\simeq \left[1 - \frac{1}{2} \langle \phi(t)^2 \rangle \right] \\ &\simeq [1 - D_r t]. \end{aligned} \quad (\text{D5})$$

Equation (D4) then becomes

$$\begin{aligned} R &\simeq \int_0^{\langle T_0 \rangle} v [1 - D_r t] dt \\ &\simeq v \left[\langle T_0 \rangle - \frac{1}{2} D_r \langle T_0 \rangle^2 \right]. \end{aligned} \quad (\text{D6})$$

Solving the above equation, we find

$$\langle T_0 \rangle \simeq \frac{R}{v} \left[1 + \frac{R}{2v} D_r \right]. \quad (\text{D7})$$

The above expression suggests that, at small D_r , $\langle T_0 \rangle$ increases linearly, starting from a nonzero value at $D_r = 0$, which is in agreement with our experimental results.

Next, we consider the large- D_r limit. Due to the interaction of the robot with light, the robot tends to maintain the value of the angle ϕ within the range $[-\pi/2, \pi/2]$, since beyond this range the light intensity I_f at the front of the robot becomes smaller than the light intensity I_b at its back. In the $D_r \gg 1/\langle T_0 \rangle$ limit, ϕ spreads out across its accessible range $[-\pi/2, \pi/2]$ long before it reaches home, thus enabling us to assume that the values of $\phi(t)$ are approximately evenly

distributed within this range. Then

$$\begin{aligned} \langle \cos \phi(t) \rangle &\simeq \frac{1}{\pi} \int_{-\pi/2}^{\pi/2} \cos \phi \, d\phi \\ &\simeq \frac{2}{\pi}. \end{aligned} \quad (\text{D8})$$

Equation (D4) then trivially gives

$$\langle T_0 \rangle = \frac{R\pi}{2v}, \quad (\text{D9})$$

which is independent of D_r , again in agreement with our experiments. Moreover, for $R/v = 4$ s, $\langle T_0 \rangle \simeq 6$ s, which impressively agrees with the experimental value of $\langle T_0 \rangle$.

We now obtain the expression of the correlation function $C_\theta(t)$ in the regime of large D_r . The first term in the ϕ equation [Eq. (D1b)] becomes less significant in this regime, allowing us to disregard it. The resulting ϕ equation becomes

$$\frac{d\phi}{dt} = \zeta(t). \quad (\text{D10})$$

We consider that $\phi = 0$ at $t = 0$ for all our trajectories, as in experiments. Then the probability distribution of ϕ at $t = 0$ is $P(\phi, 0) = \delta(\phi)$. Given that ϕ remains within the range $[-\pi/2, \pi/2]$, the probability distribution $P(\phi, t)$ of ϕ obeys the reflective boundary conditions $\partial_\phi P(\pm\pi/2, t) = 0$ conserving the probability. Implementing these boundary conditions, the expression for $P(\phi, t)$ is found to be a series expansion namely [52,53]

$$P(\phi, t) = \frac{1}{\pi} \left[1 + 2 \sum_{n=1}^{\infty} \cos 2n\phi \exp[-4n^2 D_r t] \right]. \quad (\text{D11})$$

As we have ignored the first term in Eq. (D1b), one can approximately write $\cos[\theta(t) - \theta(0)] \simeq \cos \phi(t)$. Then the temporal orientation autocorrelation function calculated using the above distribution is given by

$$\begin{aligned} C_\theta(t) &= \langle \cos[\theta(t) - \theta(0)] \rangle \\ &\simeq \langle \cos \phi(t) \rangle \\ &\simeq \int_{-\pi/2}^{\pi/2} \cos \phi P(\phi, t) \, d\phi \\ &\simeq \frac{2}{\pi} \left[1 + 2 \sum_{n=1}^{\infty} \frac{(-1)^{n-1}}{4n^2 - 1} \exp[-4n^2 D_r t] \right]. \end{aligned} \quad (\text{D12})$$

It saturates to $2/\pi$ towards large t . As mentioned in the main text, this observation closely aligns with our experimental results. The small D_r limit is rather straightforward and has been illustrated in the main text.

APPENDIX E: COMPARISON BETWEEN EXPERIMENTS AND SIMULATIONS

The main difference between the experiments and simulations is that in the simulations, the value of ϕ is stochastically reset to zero. In contrast, in the experiments, reorientation occurs only when ϕ escapes the range $[-\pi/2, \pi/2]$, and after reorientation, ϕ remains near $\pm\pi/2$. Therefore, the accessible range of ϕ in experiments is nearly $[-\pi/2, \pi/2]$. In simulations, however, ϕ remains restricted to the range $[-\Delta\phi, \Delta\phi]$,

where $\Delta\phi$ can be approximated as the root-mean-square deviation of ϕ in simulations, which decreases with increasing D_r . Then, as in Eq. (D8),

$$\langle \cos \phi(t) \rangle \simeq \frac{\sin \Delta\phi}{\Delta\phi}, \quad (\text{E1})$$

and from Eq. (D4), we find

$$\langle T_0 \rangle \simeq \frac{R}{v} \frac{\Delta\phi}{\sin \Delta\phi}. \quad (\text{E2})$$

Since the reset rate increases almost linearly with D_r [see Fig. 3(d)], $\Delta\phi (< \pi/2)$, decreases with D_r , as shown in SM Fig. S4 [54]. Then, the above equation indicates that $\langle T_0 \rangle$ in simulations is expected to decline with D_r , which is consistent with our observations in Fig. 6(d). Similarly, following the derivation of Eq. (D12), we can show that $C_\theta(t)$ saturates to a value of $\sin \Delta\phi / \Delta\phi$, which increases with D_r . This is consistent with the simulation results shown in Fig. 6(f).

APPENDIX F: MODELING AND ALGORITHM FOR HOMING SIMULATIONS WITH STOCHASTIC RESETTING SCHEME

In this section, we sketch out the details of the theoretical modeling and the simulation that was used to obtain the plots in Figs. 6(c)–6(f). There are two key ingredients to this modeling: (i) the underlying dynamics of the robot is an AB motion, and (ii) the robot experiences reorientations, which reset the angle of its movement to a particular direction. To mimic the experimental setup, we set the target to be a circular region of radius a around the center of the exploration arena with radius $R \gg a$. Starting from the circumference of the bigger circle (R) the motion continues until the simulation particle reaches the smaller circle (home/target) with radius a ; see Fig. 6(a). In what follows, we elaborate more on the two subprocesses mentioned above.

1. The underlying dynamics

The dynamic of the simulation particle is modeled as an active Brownian motion as described by the following equations

$$\begin{aligned} \dot{x}(t) &= v \cos \theta(t), \\ \dot{y}(t) &= v \sin \theta(t), \\ \dot{\theta}(t) &= \zeta(t), \end{aligned} \quad (\text{F1})$$

where $\zeta(t)$ is a Gaussian white noise with the following correlation:

$$\langle \zeta(t) \zeta(t') \rangle = 2D_r \delta(t - t'), \quad (\text{F2})$$

where D_r is the rotational diffusion constant. In simulation, one evolves the motion in discrete time steps Δt . Given the initial coordinates of the particle at time t as $(\theta(t), x(t), y(t))$ one can find the coordinates at time $t + \Delta t$ as

$$\begin{aligned} x(t + \Delta t) &= x(t) + v \cos \theta(t) \\ y(t + \Delta t) &= y(t) + v \sin \theta(t) \\ \theta(t + \Delta t) &= \theta(t) + \sqrt{2D_r \Delta t} \xi(t), \end{aligned} \quad (\text{F3})$$

where $\xi(t)$ is a Gaussian noise with zero mean and unit variance. In the simulation, the initial condition at $t = 0$ is chosen to be $\theta(t = 0) = 0$, $x(t = 0) = -R$, $y(t = 0) = 0$, where R is the radius of the circular arena in the experiment. The homing motion continues until the particle reaches inside a circle of radius a in the center of the arena. Once the homing is completed, we note the time that it takes for the active Brownian particle to reach there and repeat the simulation to estimate the statistical quantities.

2. The orientational resets

In addition to the underlying dynamics of the particle, the angle $\theta(t)$ at which it moves is reset to a prefixed direction θ_0 at random times. This random time of reorientation comes from an exponential distribution with mean $1/\nu$, i.e., the reorientations occur at a rate ν . At each time step Δt the particle reorients to θ_0 with probability (w.p.) $\nu\Delta t$ or continues to diffuse with probability $1 - \nu\Delta t$. Thus, in summary, the dynamics of the angle θ is given by

$$\theta(t + \Delta t) = \begin{cases} \theta(t) + \sqrt{2D_r\Delta t}\xi(t), & \text{w.p. } 1 - \nu\Delta t \\ \theta_0, & \text{w.p. } \nu\Delta t \end{cases} \quad (\text{F4})$$

The angle θ_0 is chosen suitably so that it makes the orientation of the particle radially inward toward the center of the circular arena.

Depending on the quadrant of the particle at a given time t , the resetting angle θ_0 can be computed using simple geometry. Following the analysis, we have

$$\theta_0 = \begin{cases} -\frac{\pi}{2} - \tan^{-1}(x/y), & \text{1st quadrant} \\ -\frac{\pi}{2} + \tan^{-1}|x/y|, & \text{2nd quadrant} \\ \tan^{-1}|y/x|, & \text{3rd quadrant} \\ \frac{\pi}{2} + \tan^{-1}|x/y|, & \text{4th quadrant} \end{cases} \quad (\text{F5})$$

In the simulation, we have set $v = 10$ cm/s, $a = 2.5$ cm, and $R = 46.25$ cm. The values of ν and D_r have been found by fitting the experimental data as shown in Fig. 3(d) to a polynomial $f(x) = \sum_i a_i x^i$ (truncated to $i = 4$). The time step Δt was chosen to be 10^{-5} s, and the results were averaged over 10^5 number of homing trajectories. The boundaries do not play a significant role in this problem since the particle

keeps correcting its direction right away from the beginning, and as such, the probability of returning toward the boundary is diminishingly small.

a. Overhead time for reorientation

In the experiment, the robot consumes a finite amount of time each time it reorients. To implement that in the simulation, we add an overhead time penalty t_r whenever a resetting/reorientation event takes place. When we neglect the reorientation times, then $t_r = 0$ and the corresponding mean homing time is shown in Fig. 6(d). Later we set t_r to be nonzero and vary its value between 0.1 and 0.9 s. The resulting statistics for the mean homing time as a function of D_r is depicted in Fig. 6(e).

APPENDIX G: CALCULATION OF $C_\theta(t)$ FROM PIGEON HOMING TRAJECTORIES

We use a publicly available empirical data repository of homing pigeons namely *Columba livia* flying in different flock sizes from the paper's Supplemental Material by Takao Sasali *et al.* [28] to calculate $C_\theta(t)$. More specifically, we used "SoloRoutes.mat" and "FlockRoutes.mat" files. The data repository contains 147 different trajectories for solo-flying pigeons, 13 trajectories for pigeons flying in flock size 2, 10 trajectories for flock size 4, and 8 trajectories for flock size 8 between home and the release site. Each trajectory has a total of three columns, where the first two columns are bird position data, and the third column is time. The data were recorded at a 5 Hz frequency with GPS loggers attached to each bird. Note the repository does not have the data for pigeons' instantaneous orientation, $\hat{\mathbf{n}}(t)$. Therefore, we assume that this vector coincides with the instantaneous unit displacement vector defined from the position data as $\hat{\mathbf{m}}(t) = \frac{1}{d(t)}[(x(t + \Delta t) - x(t))\hat{\mathbf{i}} + (y(t + \Delta t) - y(t))\hat{\mathbf{j}}]$, where $d(t) = ([x(t + \Delta t) - x(t)]^2 + [y(t + \Delta t) - y(t)]^2)^{1/2}$ is the distance traveled between t and $t + \Delta t$. We use $\Delta t = 0.2$ s as the data is recorded at 5 Hz. With this information, we calculate the temporal orientation autocorrelation function, averaged over all the available trajectories as: $C_\theta(t) = \langle \hat{\mathbf{m}}(t' + t) \cdot \hat{\mathbf{m}}(t') \rangle_{t'}$. Subscript t' on the angular brackets implies sliding average over time to improve statistics.

-
- [1] S. Mandal, How do animals find their way back home? A brief overview of homing behavior with special reference to social hymenoptera, *Insect. Soc.* **65**, 521 (2018).
- [2] F. Papi, *Animal Homing* (Springer Science & Business Media, New York, 2012).
- [3] N. Fujita, J. M. Loomis, R. L. Klatzky, and R. G. Golledge, A minimal representation for dead-reckoning navigation: Updating the homing vector, *Geogr. Anal.* **22**, 324 (1990).
- [4] V. Séguinot, R. Maurer, and A. Etienne, Dead reckoning in a small mammal: The evaluation of distance, *J. Comp. Physiol. A* **173**, 103 (1993).
- [5] S. Heinze, A. Narendra, and A. Cheung, Principles of insect path integration, *Curr. Biol.* **28**, R1043 (2018).
- [6] O. B. Stabell, Olfactory control of homing behaviour in salmonids, in *Fish Chemoreception* (Springer, Berlin, 1992), pp. 249–270.
- [7] A. Gagliardo, P. Ioale, C. Filannino, and M. Wikelski, Homing pigeons only navigate in air with intact environmental odours: A test of the olfactory activation hypothesis with GPS data loggers, *PLoS ONE* **6**, e22385 (2011).
- [8] D. Biro, R. Freeman, J. Meade, S. Roberts, and T. Guilford, Pigeons combine compass and landmark guidance in familiar route navigation, *Proc. Natl. Acad. Sci. USA* **104**, 7471 (2007).

- [9] T. S. Collett and P. Graham, Animal navigation: Path integration, visual landmarks and cognitive maps, *Curr. Biol.* **14**, R475 (2004).
- [10] R. Wiltschko and W. Wiltschko, Animal navigation: How animals use environmental factors to find their way, *Eur. Phys. J.: Spec. Top.* **232**, 237 (2023).
- [11] P. Luschi, S. Benhamou, C. Girard, S. Ciccione, D. Roos, J. Sudre, and S. Benvenuti, Marine turtles use geomagnetic cues during open-sea homing, *Curr. Biol.* **17**, 126 (2007).
- [12] J. F. Diego-Rasilla and R. M. Luengo, Celestial orientation in the marbled newt (*triturus marmoratus*), *J. Ethol.* **20**, 137 (2002).
- [13] T. W. Cronin, S. Johnsen, N. J. Marshall, and E. J. Warrant, *Visual Ecology* (Princeton University Press, Princeton, NJ, 2014).
- [14] E. Warrant and M. Dacke, Vision and visual navigation in nocturnal insects, *Annu. Rev. Entomol.* **56**, 239 (2011).
- [15] T. S. Collett, A. Wystrach, and P. Graham, Insect orientation: The travails of going straight, *Curr. Biol.* **26**, R461 (2016).
- [16] J. L. Gould and C. G. Gould, *Nature's Compass: The Mystery of Animal Navigation* (Princeton University Press, Princeton, NJ, 2012).
- [17] D. A. Wilson and R. J. Stevenson, *Learning to Smell: Olfactory Perception from Neurobiology to Behavior* (Johns Hopkins University Press, Baltimore, MD, 2006).
- [18] C. Buehlmann, P. Graham, B. S. Hansson, and M. Knaden, Desert ants use olfactory scenes for navigation, *Anim. Behav.* **106**, 99 (2015).
- [19] K. Lohmann, P. Luschi, and G. Hays, Goal navigation and island-finding in sea turtles, *J. Exp. Mar. Biol. Ecol.* **356**, 83 (2008).
- [20] P. N. Fleischmann, R. Grob, V. L. Müller, R. Wehner, and W. Rössler, The geomagnetic field is a compass cue in cataglyphis ant navigation, *Curr. Biol.* **28**, 1440 (2018).
- [21] W. S. Wilcock, K. M. Stafford, R. K. Andrew, and R. I. Odom, Sounds in the ocean at 1–100 hz, *Annu. Rev. Mar. Sci.* **6**, 117 (2014).
- [22] C. Buehlmann, B. S. Hansson, and M. Knaden, Desert ants learn vibration and magnetic landmarks, *PLoS ONE* **7**, e33117 (2012).
- [23] V. J. Coppola, G. Hough, and V. P. Bingman, Age-related spatial working memory deficits in homing pigeons (*Columba livia*), *Behav. Neurosci.* **128**, 666 (2014).
- [24] D. Costantini, G. Dell'Arciccia, and H.-P. Lipp, Long flights and age affect oxidative status of homing pigeons (*Columba livia*), *J. Exp. Biol.* **211**, 377 (2008).
- [25] J. A. Waldvogel, S. Benvenuti, W. T. Keeton, and F. Papi, Homing pigeon orientation influenced by deflected winds at home loft, *J. Comp. Physiol.* **128**, 297 (1978).
- [26] E. F. Zipkin, L. Ries, R. Reeves, J. Regetz, and K. S. Oberhauser, Tracking climate impacts on the migratory monarch butterfly, *Global Change Biol.* **18**, 3039 (2012).
- [27] J. Mehlhorn and G. Rehkaemper, The influence of social parameters on the homing behavior of pigeons, *PLoS ONE* **11**, e0166572 (2016).
- [28] T. Sasaki, N. Masuda, R. P. Mann, and D. Biro, Empirical test of the many-wrongs hypothesis reveals weighted averaging of individual routes in pigeon flocks, *IScience* **25**, 105076 (2022).
- [29] G. Dell'Arciccia, G. Dell'Omo, D. P. Wolfer, and H.-P. Lipp, Flock flying improves pigeons' homing: Gps track analysis of individual flyers versus small groups, *Anim. Behav.* **76**, 1165 (2008).
- [30] A. F. Winfield, Towards an engineering science of robot foraging, in *Distributed Autonomous Robotic Systems 8* (Springer, Berlin, 2009), pp. 185–192.
- [31] K. Sugawara, T. Kazama, and T. Watanabe, Foraging behavior of interacting robots with virtual pheromone, in *Proceedings of the IEEE/RSJ International Conference on Intelligent Robots and Systems (IROS)*, Vol. 3 (IEEE, Los Alamitos, CA, 2004), pp. 3074–3079.
- [32] A. A. Argyros, K. E. Bekris, S. C. Orphanoudakis, and L. E. Kaviraki, Robot homing by exploiting panoramic vision, *Auton. Rob.* **19**, 7 (2005).
- [33] D. Floreano and F. Mondada, Evolution of homing navigation in a real mobile robot, *IEEE Trans. Syst. Man Cybern. Part B Cybern.* **26**, 396 (1996).
- [34] S. G. Prasath, S. Mandal, F. Giardina, J. Kennedy, V. N. Murthy, and L. Mahadevan, Dynamics of cooperative excavation in ant and robot collectives, *Elife* **11**, e79638 (2022).
- [35] A. P. Solon, M. E. Cates, and J. Tailleur, Active brownian particles and run-and-tumble particles: A comparative study, *Eur. Phys. J.: Spec. Top.* **224**, 1231 (2015).
- [36] É. Fodor and M. C. Marchetti, The statistical physics of active matter: From self-catalytic colloids to living cells, *Physica A* **504**, 106 (2018).
- [37] S. Paramanick, A. Pal, H. Soni, and N. Kumar, Programming tunable active dynamics in a self-propelled robot, *Eur. Phys. J. E* **47**, 34 (2024).
- [38] N. Kumar, R. K. Gupta, H. Soni, S. Ramaswamy, and A. K. Sood, Trapping and sorting active particles: Motility-induced condensation and smectic defects, *Phys. Rev. E* **99**, 032605 (2019).
- [39] A. Kaiser, H. H. Wensink, and H. Löwen, How to capture active particles, *Phys. Rev. Lett.* **108**, 268307 (2012).
- [40] R. Di Leonardo, L. Angelani, D. Dell'Arciprete, G. Ruocco, V. Iebba, S. Schippa, M. P. Conte, F. Mecarini, F. De Angelis, and E. Di Fabrizio, Bacterial ratchet motors, *Proc. Natl. Acad. Sci. USA* **107**, 9541 (2010).
- [41] M. R. Evans and S. N. Majumdar, Diffusion with stochastic resetting, *Phys. Rev. Lett.* **106**, 160601 (2011).
- [42] A. Pal and S. Reuveni, First passage under restart, *Phys. Rev. Lett.* **118**, 030603 (2017).
- [43] A. Pal, Ł. Kuśmierz, and S. Reuveni, Search with home returns provides advantage under high uncertainty, *Phys. Rev. Res.* **2**, 043174 (2020).
- [44] M. R. Evans, S. N. Majumdar, and G. Schehr, Stochastic resetting and applications, *J. Phys. A: Math. Theor.* **53**, 193001 (2020).
- [45] A. Pal, V. Stojkoski, and T. Sandev, Random resetting in search problems, *arXiv:2310.12057*.
- [46] O. Tal-Friedman, A. Pal, A. Sekhon, S. Reuveni, and Y. Roichman, Experimental realization of diffusion with stochastic resetting, *J. Phys. Chem. Lett.* **11**, 7350 (2020).
- [47] B. Besga, A. Bovon, A. Petrosyan, S. N. Majumdar, and S. Ciliberto, Optimal mean first-passage time for a Brownian searcher subjected to resetting: Experimental and theoretical results, *Phys. Rev. Res.* **2**, 032029(R) (2020).
- [48] G. K. Sar, A. Ray, D. Ghosh, C. Hens, and A. Pal, Resetting mediated navigation of active brownian searcher in a homogeneous topography, *Soft Matter* **19**, 4502 (2023).

- [49] V. Kumar, O. Sadekar, and U. Basu, Active Brownian motion in two dimensions under stochastic resetting, *Phys. Rev. E* **102**, 052129 (2020).
- [50] E. A. Codling, M. J. Plank, and S. Benhamou, Random walk models in biology, *J. R. Soc. Interface.* **5**, 813 (2008).
- [51] V. Balakrishnan, *Elements of Nonequilibrium Statistical Mechanics* (Springer, Berlin, 2008), Vol. 3.
- [52] S. Redner, *A Guide to First-passage Processes* (Cambridge University Press, Cambridge, UK, 2001).
- [53] T. Bickel, A note on confined diffusion, *Physica A* **377**, 24 (2007).
- [54] See Supplemental Material at <http://link.aps.org/supplemental/10.1103/PRXLife.2.033007> for additional figures and supporting movie legends.